Obstacle-Aided Trajectory Control of a Quadrupedal Robot Through Sequential Gait Composition

Haodi Hu¹, Feifei Qian¹

Abstract-Modeling and controlling legged robot locomotion on terrains with densely distributed large rocks and boulders are fundamentally challenging. Unlike traditional methods which often consider these rocks and boulders as obstacles and attempt to find a clear path to circumvent them, in this study we aim to develop methods for robots to actively utilize interaction forces with these "obstacles" for locomotion and navigation. To do so, we studied the locomotion of a quadrupedal robot as it traversed a simplified obstacle field with 12 different gaits, and discovered that with each gait the robot could passively converge to a distinct orientation. A compositional return map explained this observed passive convergence, and enabled prediction of the steady-state orientation angles for each quadrupedal gait. We experimentally demonstrated that with these predictions, a legged robot could effectively generate desired shape of trajectories amongst large, slippery obstacles, simply by switching between different gaits. Our study offered a novel method for robots to exploit traditionally-considered "obstacles" to achieve agile movements on challenging terrains.

Index Terms—Legged Robots, Biologically-Inspired Robots, Dynamics, Rough Terrain Locomotion.

I. INTRODUCTION

Many terrestrial environments are filled with large obstacles such as rocks, boulders, fallen trees (Fig. 1). The ability to flexibly and efficiently move across these obstacle-dense terrains can empower legged robots for a variety of important applications, such as autonomous delivery, search and rescue [1], and planetary explorations [2]. However, ambulatory locomotion on these substrates can be highly challenging, as the sizes of these obstacles are often comparable with the robot leg size, resulting in large disturbances that could lead to a variety of potential locomotion failures, such as unexpected leg slip, stuck-in-place, large body angle fluctuation, or even flipping over [3], [4], [5], [6].



Fig. 1. Natural environments are often heterogeneous, containing large "bumps" such as fallen trees (a) or large rubble (b), which pose great challenges for legged robot locomotion. Photo materials credit iStock.

Department of Electrical and Computer Engineering, University of Southern California

Due to the complex contact dynamics, existing navigation and planning methods often rely on finding a clear path to avoid physical interactions with these large obstacles [7], [8]. For example, the artificial potential field method [9], [10] represents obstacles as repulsive potentials and goal location as attractive potentials, allowing robots to smoothly move towards the goal location while avoiding obstacles. These methods worked well for wheeled vehicles [11], [12] which often do not have the ability to cope with large obstacles. For legged robots with the extra degrees of freedom to engage large terrain heterogeneity in a diverse fashion [13], [14], [15], [16], [17], relying on obstacle avoidance could potentially limit their ability to traverse many natural terrains, where frequent interactions between legs and obstacles are unavoidable. Other methods represent these large rocks and boulders as disturbances [18], [19] to be rejected by the controller, but for terrains with large obstacles with sizes comparable with robot leg dimensions, disturbances rejection can be difficult and is often vulnerable to the sensor and actuator noises [20].

Recent robophysics [21] research has begun to explore a new direction in enabling agile locomotion among large obstacles: by actively utilizing the interaction forces between robots and obstacles, similar to mountain goats that can push against rocks to climb up steep slopes, and squirrels that use sidewalls to "parkour" and reach desired branches [22]. Recent studies on legged robots discovered that by varying body shapes [5], [23] or leg-obstacle contact positions [4], [24], legged robots could elicit different reaction forces from obstacle interactions and producing desired locomotion dynamics effectively. Similar studies in snake robots have shown that by adjusting body curvature or compliance [25], [26], snake robots could use simple controls to navigate through cluttered obstacle fields [27]. These studies suggested a new possibility for robots to generate "obstacle-aided" locomotion on terrains with large, densely-distributed heterogeneity.

To enable the next-generation robots that can intelligently adapt their locomotion strategies to achieve this obstacle-aided locomotion in challenging environments, this study seeks to answer two questions: (1) how to predict the change of robot state under leg-obstacle interactions? (2) how to select locomotion strategies to produce desired movement by utilizing obstacle interactions?

To answer these two questions, we experimentally study the orientation trajectory of a quadrupedal robot as it traversed an array of evenly-spaced obstacles. With a total of 864 experiment trials, we systematically investigate how different robot gaits, initial orientations, and initial positions, influence the passive moving direction of the robot (Sec. III). It's observed

that under the leg-obstacle interaction forces, the robot orientation exhibited a strong convergence towards quantized angles. Furthermore, the set of converged orientation angles depend primarily on robot gaits, but the robot's initial conditions (e.g., initial orientation and position) largely determine which angle the robot would converge to.

We represent this gait-dependent orientation convergence as a series of "funnels" (Fig. 2 right, a, b, c), where each robot gait couples with the obstacle field and forms one funnel that constraints robot states from a larger initial set (funnel "inlet") to a smaller final set (funnel "outlet"). We hypothesize that, by sequentially switching through a sequence of gaits, we could enable the robot to "flow" from one state (*i.e.*, previous funner outlet) to another (*i.e.*, subsequent funnel outlet) [28], and efficiently produce desired trajectories (Fig. 2 left, $a \rightarrow b \rightarrow c$) across the obstacle field without needing additional steering.

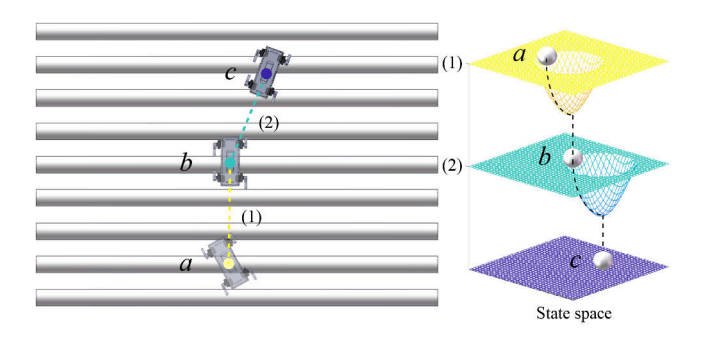


Fig. 2. Conceptual illustration of a robot achieving desired orientation trajectories (left diagram) by moving through a number of "funnels" (right diagram). With each gait (left diagram, (1) and (2)), the robot would passively converge to different steady-state orientations (b, c) under the leg-obstacle interaction forces. We represent this convergence as a constraining "funnel", where a robot starting from a certain initial state that belongs to the "inlet" of the funnel would passively flow towards the corresponding "outlet" of the funnel (i.e., the steady state) of a certain gait. By connecting one funnel after another (i.e., yellow, cyan, purple in the right diagram), with the outlet of the previous funnel positioned within the inlet of the next funnel, a robot could passively move through desired states a, b, c by sequentially executing gait (1) and (2).

To predict the gait-dependent converged orientations (*i.e.*, Fig. 2 right, funnel outlets) and their connections with the corresponding initial conditions (*i.e.*, Fig. 2 right, funnel inlets), we propose a general method that computes a gaitwise return map of robot state transitions for given environment and gait parameters. We show that the return map can explain the observed state convergence, and enable theoretical prediction of obstacle-modulated steady states for any general, quadrupedal gaits (Sec. IV). Using the model-predicted funnel inlets and outlets, we demonstrate experimentally that by sequentially switching through a sequence of gaits, a simple (microcontroller-based) legged robot could utilize leg-obstacle collision forces to generate desired trajectory across densely-distributed large obstacles (Sec. V).

II. MATERIALS AND METHODS

To obtain a better understanding of the robot locomotion under repeated leg-obstacle collisions, we studied the horizontal-plane dynamics of a quadrupedal robot as it ran across an obstacle field with systematically-varied gaits and initial conditions (*i.e.*, orientations and positions).

A. Robot and Gaits

The robot used in this study is a small RHex-class [14] robot (Fig. 3a), with a body length of 16.5 cm, a body width of 15.2 cm, and a total weight of 1.4 kg. Four rotary C-shaped robot legs were 3D printed (PLA plastic) with an outer diameter of 6 cm. All legs were actuated with servo motors (Lynxmotion LSS-ST1), and controlled by a microcontroller (Arduino Uno). The gait frequency was kept at 0.33Hz for all experiments in this study. The phase of a leg i, $\beta_i(t) \in [0,T)$, was defined as the relative place of time, t, during a full gait cycle, T. Here the leg index $i \in H$, where $H = \{LF, RF, LH, RH\}$ represents the set of robot legs (left front, right front, left hind, right hind, respectively). For a quadrupedal robot, a periodic gait can be uniquely specified using the phase difference between any three pairs of legs [29], [30], [31].

To represent general quadrupedal gaits, we construct a gait space [29] (Fig. 3c), (ϕ_1, ϕ_2, ϕ_3) :

$$\phi_1 = (\beta_{LF} - \beta_{RF}) \% T$$

$$\phi_2 = (\beta_{LH} - \beta_{RF}) \% T$$

$$\phi_3 = (\beta_{RH} - \beta_{RF}) \% T$$
(1)

Here $\phi_i \in [0,T)$ represents the phase difference between the LF-RF, LH-RF, and RH-RF leg pairs (Fig. 3b). Each point in the gait space, (ϕ_1,ϕ_2,ϕ_3) , represents a periodic quadrupedal gait. Within the gait space (Fig. 3c), the three lines $(0,\phi_0,\phi_0)$, $(\phi_0,0,\phi_0)$, and $(\phi_0,\phi_0,0)$ represents the groups of "virtual-bipedal" (VB) gaits [32], where two of the four legs function as a synchronous pair, and alternate with the other two synchronous legs. Previous study [33], [34] has found that two specific virtual bipedal gaits (Fig. 3c, G_1 and G_5) could allow an open-looped robot to passively maintain a consistent moving direction across evenly-spaced obstacle field. In this study, to extend this understanding to general quadrupedal gaits, we experimentally studied a total of 12 gaits, G_1 to G_{12} (Fig. 3 c), to investigate how different gaits affect robot trajectories within the obstacle field:

$$G_{1}: (\phi_{1}, \phi_{2}, \phi_{3}) = (0, 0.5T, 0.5T)$$

$$G_{2}: (\phi_{1}, \phi_{2}, \phi_{3}) = (0.125T, 0.375T, 0.5T)$$

$$G_{3}: (\phi_{1}, \phi_{2}, \phi_{3}) = (0.25T, 0.25T, 0.5T)$$

$$G_{4}: (\phi_{1}, \phi_{2}, \phi_{3}) = (0.375T, 0.125T, 0.5T)$$

$$G_{5}: (\phi_{1}, \phi_{2}, \phi_{3}) = (0.5T, 0, 0.5T)$$

$$G_{6}: (\phi_{1}, \phi_{2}, \phi_{3}) = (0.5T, 0.125T, 0.375T)$$

$$G_{7}: (\phi_{1}, \phi_{2}, \phi_{3}) = (0.5T, 0.25T, 0.25T)$$

$$G_{8}: (\phi_{1}, \phi_{2}, \phi_{3}) = (0.5T, 0.375T, 0.125T)$$

$$G_{9}: (\phi_{1}, \phi_{2}, \phi_{3}) = (0.5T, 0.5T, 0)$$

$$G_{10}: (\phi_{1}, \phi_{2}, \phi_{3}) = (0.375T, 0.5T, 0.125T)$$

$$G_{11}: (\phi_{1}, \phi_{2}, \phi_{3}) = (0.25T, 0.5T, 0.375T)$$

$$G_{12}: (\phi_{1}, \phi_{2}, \phi_{3}) = (0.125T, 0.5T, 0.375T)$$

All gaits from G_1 to G_{12} are defined with $\beta_{RF}=0.5T$. Among them, Gait G_1 , G_5 , G_9 are virtual bipedal (VB) gaits.

 $^{^{1}\}mathrm{We}$ use the symbol % to denote a modulo operation.

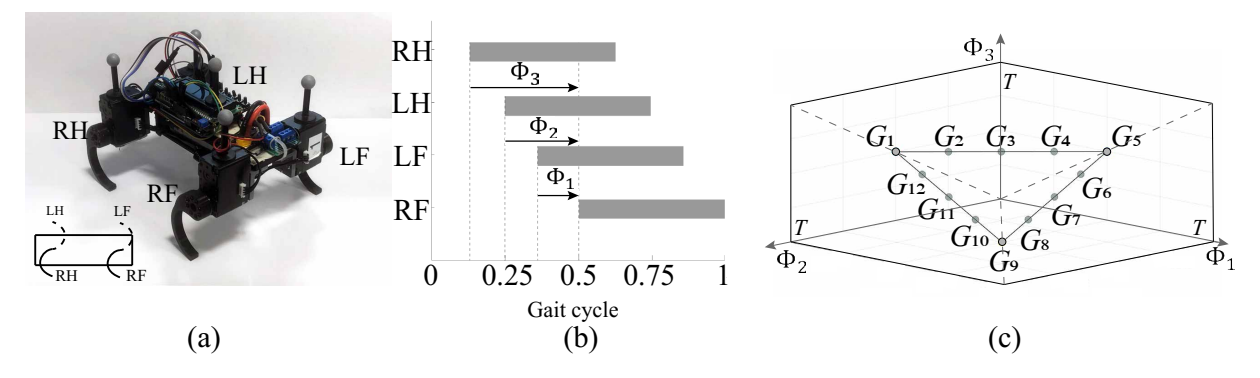


Fig. 3. Quadrupedal robot (a) and two representations of robot gaits: gait diagram (b) and gait space (c). LF, RF, LH, RH in (a) and (b) represent the four legs of the robot: left-front (LF), right-front (RF), left-hind (LH), and right-hind (RH), respectively. Gray regions in (b) represent the stance duration of each leg within one gait cycle. ϕ_1 , ϕ_2 , ϕ_3 in (b) represent the phase differences between the LF and RF legs, LH and RF legs, and RH and RF legs, and the span of (ϕ_1, ϕ_2, ϕ_3) forms the three gait axes. Every point within $\phi_i \in [0, T), i = 1, 2, 3$ represents a unique periodic quadrupedal gait of a quadrupedal robot. The three dash lines represent the three groups of virtual bipedal gaits. G_1 to G_{12} indicate the 12 gaits tested in our experiments. Inset in (a) shows a side view of the robot with gait G_9 , where leg RH has a relative phase of $\phi_3 = 0$ with leg RF, and the two left legs, LF and LH, are half-cycle out of phase with the RF leg, i.e., $\phi_1 = 0.5T$, $\phi_2 = 0.5T$.

Specifically, gait G_1 is a commonly-observed gait among quadrupedal animals, "bound", where two front legs (LF and RF) move synchronously and with half a cycle out of phase with two hind legs (LH and RH). Gait G_5 is another commonly-observed biological gait, "trot", where two legs within a diagonal pair (LH and RF, LF and RH) move synchronously and out of phase with the other pair. Gait G_9 is commonly referred to as "pace", where two left legs (LF and LH) form a synchronous pair and half a cycle out of phase with the two right legs (RF and RH). The rest of the 9 gaits $(G_2, G_3, G_4, G_6, G_7, G_8, G_{10}, G_{11}, G_{12})$ are "non-virtualbipedal" (NVB) gaits, where each individual leg (LF, RF, LH, RH) enters the stance phase at a different time. We chose to include G_1 and G_5 as they have been found to exhibit passively steady-state orientations [33]. By investigating the other gaits (especially the NVB gaits), we seek to uncover the general principles that governs the obstacle-modulated robot trajectories, and develop a model that can predict the robot trajectories for any general quadrupedal gait.

B. Obstacle field

The interaction between the robot legs and the obstacle arrays can be extremely complicated – it was discovered in a previous study [3] that even a small difference in initial position could lead to significantly different robot trajectories within only a few steps. For this reason, directly modeling the robot dynamics on completely random obstacle environment can be difficult. To begin to obtain a better understanding of what governs the robot dynamics as it runs through these large obstacles, we used a simplified obstacle field – an array of evenly-spaced half-cylindrical obstacles – to study the effect of gait on robot-obstacle interactions (Fig. 4). The obstacle diameter (D = 4.8 cm) was comparable with the size of the robot leg, such that the obstacles are large enough to generate large perturbation to re-oriented or re-position the robot. The obstacle spacing (P = 4 cm) was smaller than the robot's step length, such that the robot would encounter leg-obstacle collisions at every step, allowing investigation of the obstaclemodulated robot dynamics. The periodic structure of obstacles

reduces the uncertainty in repeated leg-obstacle collisions and allows stable interaction patterns (Sec. III) to emerge, while general understanding from the simplified obstacle field could be extended to different obstacle spacing [33] and more complex obstacle shapes [3].

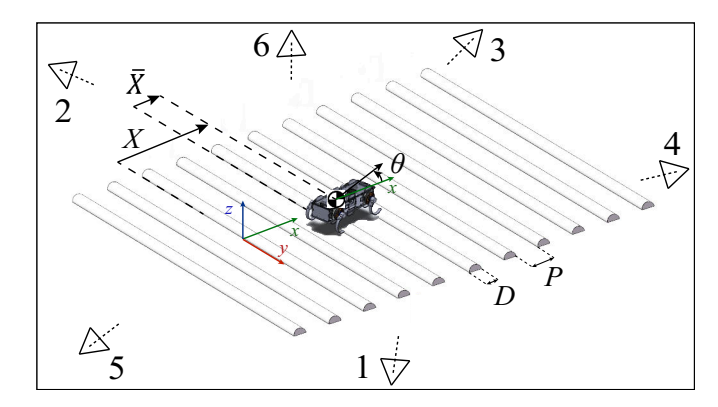


Fig. 4. Experiment setup of an open-loop, quadrupedal robot traveling through an array of evenly-spaced half-cylindrical shape obstacles with a fixed gait, G_i , $i \in \{1, 2, ..., 12\}$. Triangles represent camera positions. Cameras 1-4 were used to track the robot CoM position (X, Y, Z) and body angles (pitch, yaw, roll) during the obstacle field traversal. Cameras 5 and 6 were used to provide robot-obstacle interaction videos from the front view and top view. P and D represent obstacle spacing and diameter, respectively. θ , represents the robot yaw angle measured counter-clockwise from the x direction.

C. Experiment procedure

To understand how changes in robot orientation and trajectory are related to leg-obstacle contact positions, we measure robot kinematics in the horizontal plane of the world frame, including center-of-mass (CoM) position, (X, Y), and orientation, θ (Fig. 4), as the robot traverses the obstacle field. Four cameras (Optitrack Prime 13W) were installed at the four corners of the experiment arena to track robot kinematics, and two additional cameras (Optitrack Prime Color) are used to obtain experiment videos. Both tracking data and video are recorded at a frame rate of 120 frames per second (FPS).

At the beginning of each trial, the robot was placed within the obstacle field with an initial orientation, θ_0 , and initial position, X_0 . Due to the constant obstacle shape profile along the y-axis, robot dynamics was insensitive to its lateral position, Y, and thus Y_0 was kept at 0 for all trials. For each trial, the robot was set to traverse the obstacle field with a fixed periodic gait and without any sensory feedback or steering control, which allows us to observe the change of robot orientation and trajectory as a result of the physical interactions between robot legs and the obstacle field. Each trial was recorded for 20 seconds, or until the robot exited the range of the obstacle field (5m long x 3m wide). Robot final orientation, θ_f , was computed as the averaged robot orientation from the last two gait cycles (i.e., the last 6 seconds of the trial).

We performed experiments for 12 robot gaits, G_1 to G_{12} (Eqn. 2). Each gait was tested with 16 different robot initial orientations, where θ_0 was systematically varied from 0° to 75° with an increment of 5° . For initial orientation larger than 75° , the robot would run sideways towards 90° regardless of gaits for most trials, whose mechanism was trivial [24] and therefore not included in the discussion of this paper. Empirical measurements in [3], [24] suggested that the magnitude and direction of obstacle disturbances depended primarily on the inclination angle at the relative contact position on each obstacle. Due to the periodic distribution of the obstacles in our study, the obstacle inclination is a one-dimensional periodic function along the x direction, with a spatial period, P+D, of 8.8 cm, measured from the edge of one obstacle to the next. Here we use \bar{X} to denote the relative robot CoM position,

X, within each spatial period: $\bar{X}:=X~\%~(P+D)$. For experiments with all gaits, we started the robot within the obstacle field with $\bar{X}_0=0$ cm. To understand the effect of initial relative position on robot final orientation, θ_f , we tested gait G_1, G_5 and G_9 with two additional \bar{X}_0 , at 1 cm and 5 cm. We collected 3 trials each for each combination of gait, initial orientation, and initial relative position, resulting in a total of 864 trials.

III. EXPERIMENTAL RESULTS

A. Dependence of robot final orientation on gait

We observed a strong convergence of robot orientation towards specific final orientations for all 12 gaits. Fig. 5 shows the experimentally-measured robot trajectory (Fig. 5b) and orientation (Fig. 5c) for three of the gaits tested: G_1 , G_{11} , and G_9 . Among the 144 trials with the G_1 gait (Fig. 5c, top row), the robot orientation passively converged to $0^{\circ} \pm 1^{\circ}$ in 36 trials (25%), $35^{\circ} \pm 5^{\circ}$ in 81 trials (56%), and $85^{\circ} \pm 6^{\circ}$ in 27 trials (19%). Among the 48 trials with the G_{11} gait (Fig. 5c, middle row), the robot orientation converged to $-19^{\circ} \pm 3^{\circ}$ in 6 trials (13%), $19^{\circ} \pm 3^{\circ}$ in 17 trials (35%), $45^{\circ} \pm 7^{\circ}$ in 14 trials (29%), and $68^{\circ} \pm 4^{\circ}$ in 11 trials (23%). Similarly, among the 144 trials with the G_9 gait (Fig. 5c, bottom row), robot orientation passively converged to $7^{\circ} \pm 10^{\circ}$ in 69 trials (48%), $49^{\circ} \pm 5^{\circ}$ in 72 trials (50%), and $82^{\circ} \pm 2^{\circ}$ in 3 trials (2%). In most trials, the robot orientation converges to these passively stable steady states within the first few seconds of leg-obstacle interactions. Note that we did not perform any body-level steering, and therefore the observed convergence

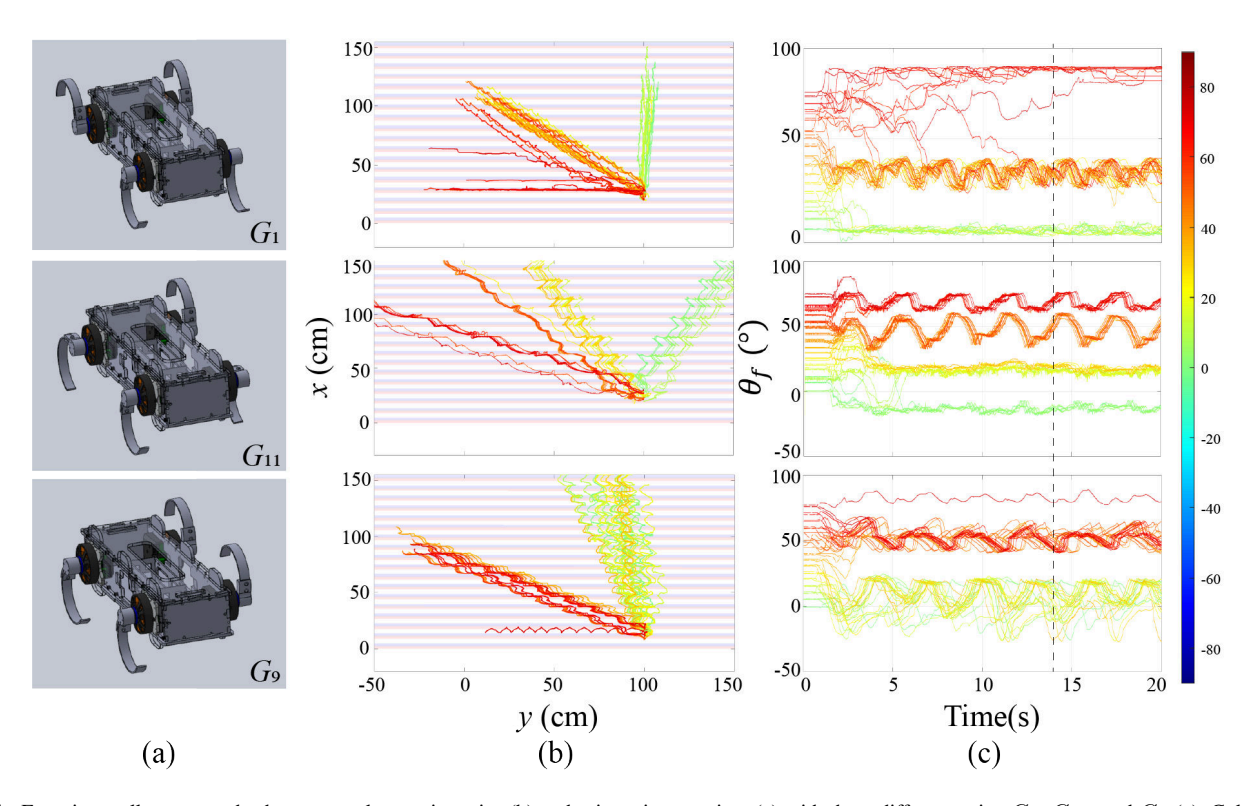


Fig. 5. Experimentally measured robot x-y plane trajectories (b) and orientation v.s. time (c) with three different gaits: G_1 , G_{11} , and G_9 (a). Colors in (b) and (c) represent different initial orientations, θ_0 , as shown in the color bar. Vertical dashed lines in (c) indicate the starting time of the last two gait cycles where the averaged final orientation, θ_f , was computed.

of robot orientation is a result of physical collisions between robot legs and obstacles.

Fig. 11 shows the experimentally-measured θ_f (red shaded area) for all 12 gaits. The quantized final orientations suggested that robot gait contributes significantly to determining the obstacle-modulated robot dynamics. More interestingly, different gait would send the robot towards different passively-stable moving directions, providing the possibility for a robot to navigate itself across obstacle fields by adapting its gait.

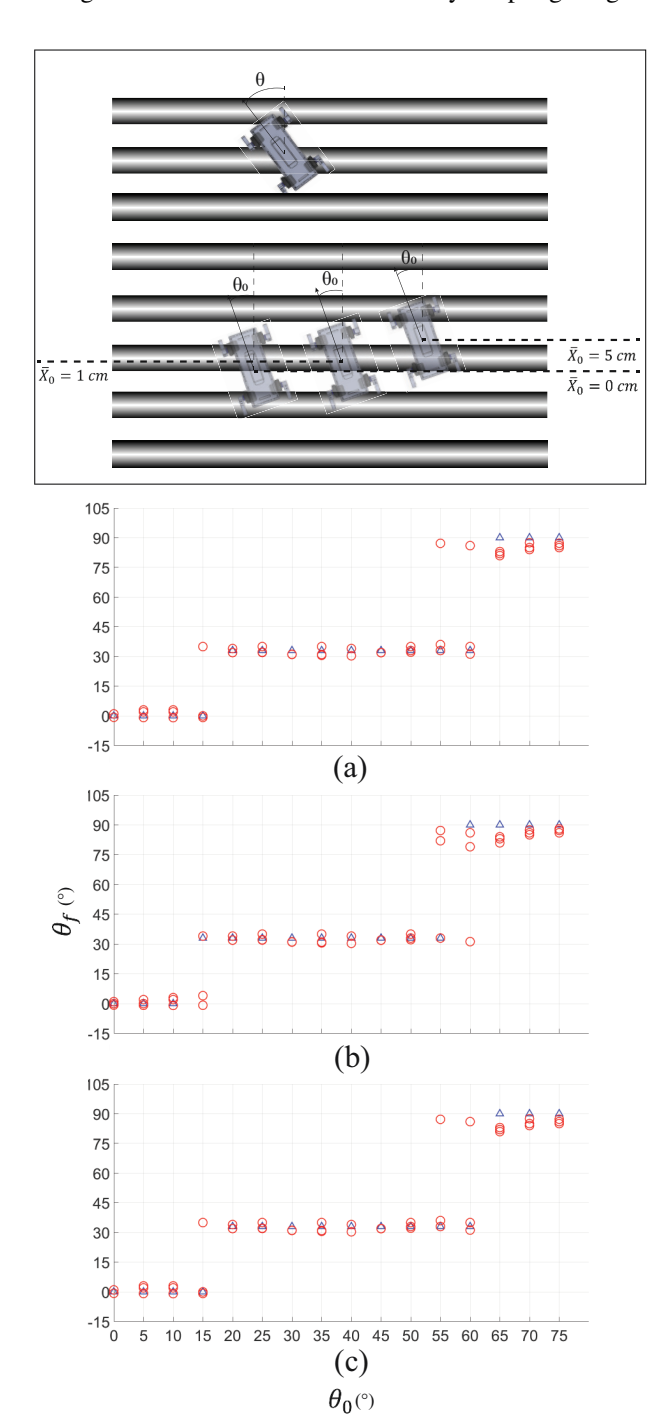


Fig. 6. Averaged final orientation, θ_f , versus initial orientation, θ_0 , for gait G_1 , with three initial positions: $\bar{X}_0 = 0$ cm (a), 1 cm (b), and 5 cm (c). Red circles represent experiment measurements. Three trials were performed for each initial condition. Blue triangles represent model predictions.

B. Dependence of robot final orientation on initial orientation and position

With each robot gait, there could exist multiple steady-state orientations, θ_f (Fig. 5c). Which θ_f the robot would converge to depended primarily on the initial condition. Fig. 6 shows the experimentally-characterized θ_f for a representative gait, G_1 , with three different initial positions: $\bar{X}_0 = 0$ cm (Fig. 6a, red circles), 1 cm (Fig. 6b, red circles), and 5 cm (Fig. 6c, red circles). For each \bar{X}_0 , trials from 16 different initial orientations, θ_0 , were plotted.

Based on Fig. 5c, there existed three primary steady-state orientations for G_1 : 0° , 35° and 85° . We noticed that trials starting with initial robot orientations within $0^{\circ} \sim 10^{\circ}$, $35^{\circ} \sim 55^{\circ}$, and $70^{\circ} \sim 75^{\circ}$, would converge to 0° , 35° , and 85° , respectively (Fig. 6). However, with initial orientation within $10^{\circ} \sim 35^{\circ}$ and $55^{\circ} \sim 70^{\circ}$, robot could converge to different final orientations depending on its initial relative position, \bar{X}_0 (Fig. 6a, b, c).

We hypothesized that both the gait-dependent steady-state orientations, and their corresponding basins of attraction, were results of different leg-obstacle contact patterns set by the robot gait. To understand how different gaits map initial robot states to passively stable steady states, in Sec. IV we use a compositional return map to investigate the convergence of robot dynamics under leg-obstacle collision forces.

IV. MODEL REVEALED ROBOT ORIENTATION CONVERGENCE MECHANISM

To reveal the mechanisms behind the experimentallyobserved convergence of robot orientations and their dependence on robot gaits, we leveraged an obstacle disturbance selection (ODS) framework [33] to compute the robot state transitions under obstacle collisions (Sec. IV-A). The concept of obstacle disturbance selection was recently introduced to connect individual leg-obstacle contacts with the robot body dynamics. By representing obstacles as a horizontal-plane force field, and representing robot legs as obstacle disturbance "selectors", the ODS framework is useful in connecting the leg-obstacle contact position patterns [24] with the obstacle reaction forces and the robot dynamics. In this study, we expanded the ODS framework to understand the effect of general quadrupedal gaits on obstacle-modulated robot dynamics. First, we leveraged the ODS force model [33] to compute the change of robot's position and orientation due to the obstacle forces exerted at each leg (Sec. IV-B). We show that obstacle forces from all obstacle-contacting legs can be composed to estimate the change of robot state during multileg, multi-obstacle contact events (Sec. IV-C) for a given gait. Composition of multiple contact events within a stride yielded a return map (Sec. IV-D) that revealed how gait patterns affected the robot state convergence (Sec. IV-F), and provided a simple method for predicting gait-dependent steady-state robot orientations (Sec. IV-E).

A. Representing obstacles as a horizontal-plane force field, and robot legs as obstacle force selectors

The ODS framework [33] represented physical obstacles as a horizontal-plane² force field. According to empirical measurements from [3], the horizontal-plane obstacle forces from each individual leg, F_i , could be computed as a function of the obstacle inclination angle, γ , at the leg-obstacle contact position, \bar{X}_i (Fig. 7a, b). The direction of F_i depended on which side of obstacles the leg contacted: F_i pointed forward (i.e., along the +x direction) for $\bar{X}_i \in (D/2, D)$, and pointed backward (i.e., along the -x direction) for $\bar{X}_i \in (0, D/2)$.

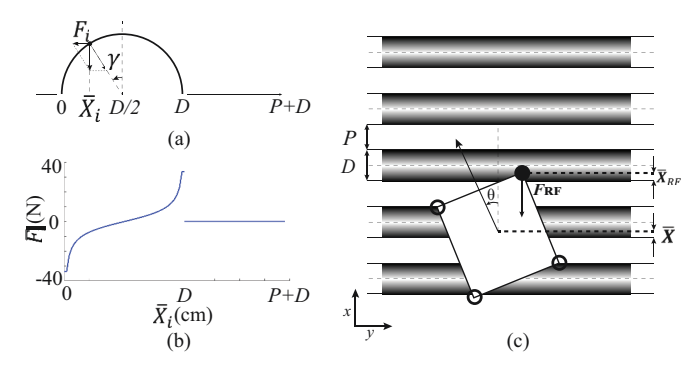


Fig. 7. The ODS representation of the obstacles (a, b) and the robot (c). (a) shows a cross-section view of the half-cylindrical obstacle, where γ denotes the obstacle inclination angle at \bar{X}_i , and F_i denotes the horizontal-plane obstacle force at \bar{X}_i . The obstacle force, F_i , as a function of \bar{X}_i , is shown in (b). (c) shows the ODS representation of a multi-legged robot. The black rectangle represents the robot body, and the black circular markers at the rectangle vertices represent the four legs of the robot. Solid circle represents the leg in the stance phase, whereas open circles represent the legs in the swing phase. Gray-shaded regions indicate the location of half-cylindrical obstacles, where the parallel solid lines indicate obstacle edges, and the dashed lines indicate the obstacle center.

The robot body was approximated as a rectangle in the x-y plane (Fig. 7c). Each robot leg was modeled as "obstacle force selectors" that attached at the vertices of the rectangle and select the obstacle disturbances, F_i , available at their positions, \bar{X}_i . To simplify the complexity of the model and capture the dominating effects, the C-shape legs were represented as points fixed at the hip joints, whereas the actual leg shape or the periodic movement of the toe relative to the hip were not specifically modelled.

We note that our goal was not to develop a high-fidelity simulation that captures all physical details. Instead, we seek to use a highly-simplified model to capture the dominant effect that governs the obstacle-modulated robot orientations. Therefore, we make several simplifying assumptions and approximations, such as neglecting actual leg shape, body pitching/rolling, and inertial effect. It has been demonstrated in [33] that despite these simplifications, the ODS model could successfully capture experimentally-measured robot steady-state orientations under the influence of leg-obstacle collisions.

B. Representing interaction opportunities from each individual leg

Using the ODS representation, we computed the change in robot states when an individual leg contact with an obstacle. Due to the symmetry along the y direction and the periodicity along the x direction, the horizontal-plane robot state could be described using a reduced state space, (θ, \bar{X}) . Here $\theta \in [-\pi, \pi)$ is the yaw angle of the robot body, measured counter-clockwise from the x-axis of the world frame, and \bar{X} is the robot CoM relative position within one spatial period of the obstacle field, P+D. Given a robot state, (θ, \bar{X}) , each individual leg's position in the world frame, x_i , and the corresponding obstacle force, $F_i(x_i)$, can be determined. The rotational and translational acceleration of the robot body, caused by the obstacle forces from an individual leg, i, can be expressed as:

$$\ddot{\theta} = \frac{F_i \cdot y_i - T_d}{I},\tag{3}$$

$$\ddot{X} = \frac{F_i - F_d}{m}. (4)$$

Here y_i represents the y-axis position of robot leg i relative to its CoM. F_d and T_d represents the damping force and torque, computed as $F_d = c_1 \cdot \dot{X}$, and $T_d = c_2 \cdot \dot{\theta}$. Damping coefficients $c_1 = 29.6$ and $c_2 = 0.097$ were obtained by matching the model-computed robot forward speed and orientation convergence rate with experimental measurements, and kept constant across all gaits and trials. I represents the moment of inertia of the robot, computed based on uniform weight distribution.

By integrating Eqn. 3 and Eqn. 4 for a fixed time duration, δt , we could generate vectors showing how the robot state (θ, \bar{X}) , would change, when a single leg engages with the obstacles. We refer to these vectors as the state transition vectors, defined as the vector pointing from the robot's current position and orientation, (θ_0, \bar{X}_0) , to the position and orientation that the robot would reach after a short duration, assuming no initial angular and linear body velocities $\dot{\theta}=0, \dot{X}=0$.

Note that the state transition vectors could be significantly different (Fig. 8a, b, c, d) if a different robot leg were to contact the obstacles. Fig. 8 illustrates the state transition vectors computed with $\delta t = 0.3$ seconds, the estimated time of leg-obstacle contact during our experiments. In this example, we can see that if the RF leg were to engage with the obstacle (Fig. 8e), the obstacle force would result in a clockwise (CW) rotation in robot orientation, θ , from 0° to -10° (Fig. 8a, θ component of the blue vector), and a decrease in robot's relative position, \bar{X} , from 3.0 cm to 1.6 cm (Fig. 8a, \bar{X} component of the highlighted vector). However, if the LF leg were to engage with the obstacle (Fig. 8f), the obstacle force would result in a counter-clockwise (CCW) rotation in robot orientation, θ , from 0° to 10° (Fig. 8b, θ component of the blue vector), and a decrease in robot's relative position, \bar{X} , from 3.0 cm to 1.6 cm (Fig. 8b, \bar{X} component of the highlighted vector). Similarly, if leg LH (Fig. 8c, g) or RH (Fig. 8d, h) were engaged with obstacles, the robot would transition towards different states under the leg-obstacle interaction forces.

²The general expression of the horizontal force field is F(X,Y). In this study, due to the symmetry of obstacle shape along the y direction and the periodicity along the x direction, the obstacle force only depends on the relative position of the leg-obstacle contact point, \bar{X}_i , and is therefore denoted as $F_i(\bar{X}_i)$.

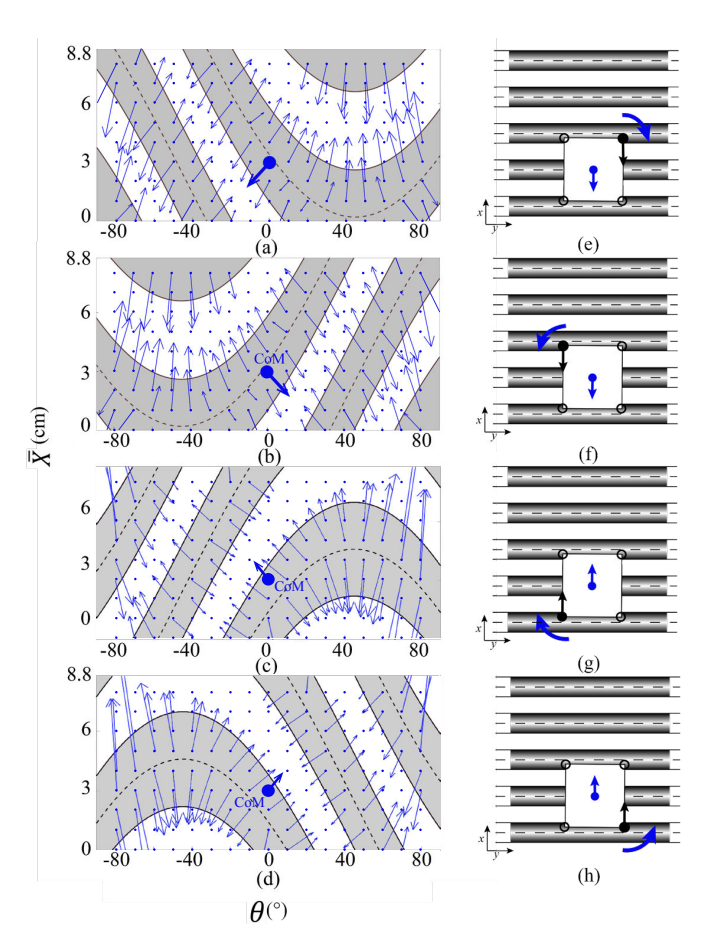


Fig. 8. Robot state transition vectors when only one individual leg (a, e -RF; b, f - LF; c, g - LH; d, h - RH) were to engage with the obstacle, shown in the robot's state space (a, b, c, d) and the world frame (e, f, g, h). Blue arrows in (a, b, c, d) represent the state transition vectors. Blue solid circles represent a representative robot's initial state, (θ_0, \bar{X}_0) . Curved and straight blue arrows in (e, f, g, h) illustrate the change in robot state corresponding to the state transition arrows from (θ_0, \bar{X}_0) in (a, b, c, d), highlighted with the thick blue arrows. The state transition vectors were displayed for a discrete set of initial conditions, for robot orientations $\theta \in [-80^{\circ}, 80^{\circ}]$ with a resolution of 10° , and robot positions $\bar{X} \in [0, P + D)$ with a resolution of 1cm. State transition vectors for robot orientation outside [-80°, 80°] were computed similarly but were not displayed. In (a-h), grey-shaded regions represent the location of obstacles; solid horizontal lines represent obstacle edges; and dashed horizontal lines represent obstacle center lines. In (e, f, g, h), black rectangles represent the robot body, and circles at the vertices of the rectangle represent the robot legs. Black solid circles represent robot legs in the stance phase, whereas black empty circles represent legs in the swing phase.

The implication is that, by selecting which leg to engage with obstacle interactions, a robot could elicit different obstacle forces from the same environment and move towards desired directions. To this end, the plots in Fig. 8a-d represents the interaction opportunity from each individual leg.

C. Computing robot state transitions under multi-leg obstacle interactions

In this section, we use the state transition vectors from each leg to compute how the robot state would change when multiple legs contact the obstacles simultaneously.

Based on the ODS framework [33], the total obstacle force and torque exerted on the robot body can be computed as a sum of forces and torques from each obstacle-contacting leg.

As a result, when multiple legs contact with obstacles, Eqn. 3 and Eqn. 4 became

$$\ddot{\theta} = \sum_{i \in S(t)} \frac{F_i \cdot y_i - T_d}{I},\tag{5}$$

$$\ddot{X} = \sum_{i \in S(t)} \frac{F_i - F_d}{m},\tag{6}$$

where $S(t) = \bigcup S_i(t)$ represents the collection of legs that are subjected to obstacle disturbances at time t. $S_i = 1$ indicates that a leg i, $i \in \{RF, LF, LH, RH\}$ is in the obstacle-contacting phase and would "select" the F_i available at its current position, and $S_i = 0$ indicates that a leg i is re-circulating, and thus would not be subjected to F_i at its position.

By integrating Eqn. 5 and Eqn. 6 over a short³ duration, δt , the changes in robot state under multi-leg, multi-obstacle interactions could be estimated from the individual leg-obstacle contact forces. Fig. 9c illustrates the state transition vectors when two legs, LH and RH, were simultaneously in contact with obstacles. As highlighted by the thick black arrow, from a given initial state, $(\theta_0, \bar{X}_0) = (35^\circ, 2.7 \text{ cm})$ (Fig. 9c, B_3), the robot state would transition toward $(\theta, \bar{X}) = (30^\circ, 1.6 \text{ cm})$ (Fig. 9c, B_4), under the obstacle forces from both LH and RH legs. This is consistent with the observations from our experiments (Fig. 12c-iv), where the robot body was observed to rotate clockwise (Fig. 9g, curved blue arrow) and slipped backward slightly (Fig. 9g, straight blue arrow) upon the LH and RH leg touchdown.

The robot could produce significantly different dynamics if a different group of legs (e.g., Fig. 9a, leg RF and LF; versus Fig. 9c, leg RH and LH) were to touchdown simultaneously. This began to reveal the observed effect of gait on obstacle-modulated robot dynamics: As robot gait varies, the grouping of obstacle-contacting legs changes. As a result, the multilegged robot could passively "flow" toward different states under the obstacle interaction forces.

D. Representing obstacle-modulated robot dynamics as a gaitdependent, compositional return map

In this section, we compose the state transition vectors into a return map to predict the robot's steady states under repeated leg-obstacle interactions.

We represented the effect of gait on robot dynamics as a sequence of leg-obstacle interaction events (which we referred to as "modes"). Each leg-obstacle interaction event ("mode") functioned as a map that sent the robot state at the beginning of the interaction, to the robot state at the end of the interaction. Composing the modes during the entire stride cycle yielded the stride-wise return map [35], [36], F, that sent the robot state from one stride to another.

For a general quadrupedal gait, each stride cycle comprised up to four steps, with each step beginning with a leg touchdown event. For example, for a VB gait like G_1 , each stride

 3 Numerical simulation suggested that the model-predicted robot steady-state orientations were insensitive to the selection of δt values for $\delta t \leq 0.9s.$ For all results reported in this paper, δt was set to 0.3 s.

cycle comprised of two steps: (i) step one, where the RF and LF legs (Fig. 9e, solid circles) simultaneously touched down, at the beginning of each stride cycle (t=0); (ii) step two, where the LH and RH legs (Fig. 9g, solid circles) simultaneously touched down half a cycle later (t=T/2). Each step can be further divided into two modes: (i) a "slipping" mode, S, where the leg initially contacted with the obstacle, and the robot's orientation and position could change significantly during a short period of time as the contacting legs slipped off the obstacles; (ii) an "advancing" mode, V, where the legs have slipped off the contacting obstacles, and the robot moved forward along its current heading.

As such, the stride-wise return map for G_1 can be represented as the composition of the four mode maps: $F = S_1 \circ V_1 \circ S_2 \circ V_2$, where S_n represents the mapping of robot state from the touchdown to the end of the slipping for the n-th step, and V_n represents the mapping of robot state from the end of slipping to the beginning of the next touchdown for the n-th step.

The mode maps can be readily computed from the state transition vectors. Fig. 9 illustrates the robot state transition vectors corresponding to the four modes, for a VB gait, G_1 . The slipping mode maps, S_1 (Fig. 9a) and S_2 (Fig. 9c), were computed as the robot state transition vectors from the active (i.e., in stance) legs (leg LF and RF for S_1 , leg LH and RH for S_2). The advancing mode maps, V_1 and V_2 (Fig. 9b, d, blue arrows), was computed as a linear displacement along the robot's current orientation. The magnitude of the advancing map vector was computed from the experimentally-measured robot stride length on flat ground scaled by the duration of the advancing mode within a full stride, then projected to the world frame.

The stride-wise return map for any general gait can be computed similarly. Fig.10 illustrates the state transition vectors for a NVB gait, G_{11} . For G_{11} , each stride consists three leg touchdown events: RF (at t = 0), LH (at t = 0.5T), LF and RH (at t = 0.75T). Each touchdown event started with the slipping mode (where the robot orientation changes significantly as the touchdown leg slides off the obstacle) and followed by an advancing mode (where the obstacle force from the touchdown legs no longer contributes significantly to the body yaw). Therefore, for G_{11} , F is composed of 6 modes: $F = S_1 \circ V_1 \circ S_2 \circ V_2 \circ S_3 \circ V_3$, where S_1 and V_1 , S_2 and V_2 , S_3 and V_3 correspond to the robot state transition upon the touchdown of {RF}, {LH}, {LF, RH}, respectively. For S_1 (Fig.10a) and S_2 (Fig.10c), the state transition vectors are the same as those from single leg RF and LH (Fig.8a, c). For S_3 (Fig. 10e), the state transition vectors were computed as a vector addition from LF and RH legs' state transition vectors (Fig.8b, d). Similar to the VB case, the advancing modes, V_1 , V_2 , V_3 , were computed as the experimentally-measured flatground stride length scaled by the duration of the advancing mode $(0.5T \text{ for } V_1, 0.25T \text{ for } V_2, 0.25T \text{ for } V_3)$. For both VB and NVB gaits, the initial angular and linear body velocities were assumed to be zero at the beginning of each mode.

Representing robot state transitions in the state space allows the features of the environment (e.g., obstacle dimension and distribution) and the robot morphology (e.g., dimension and

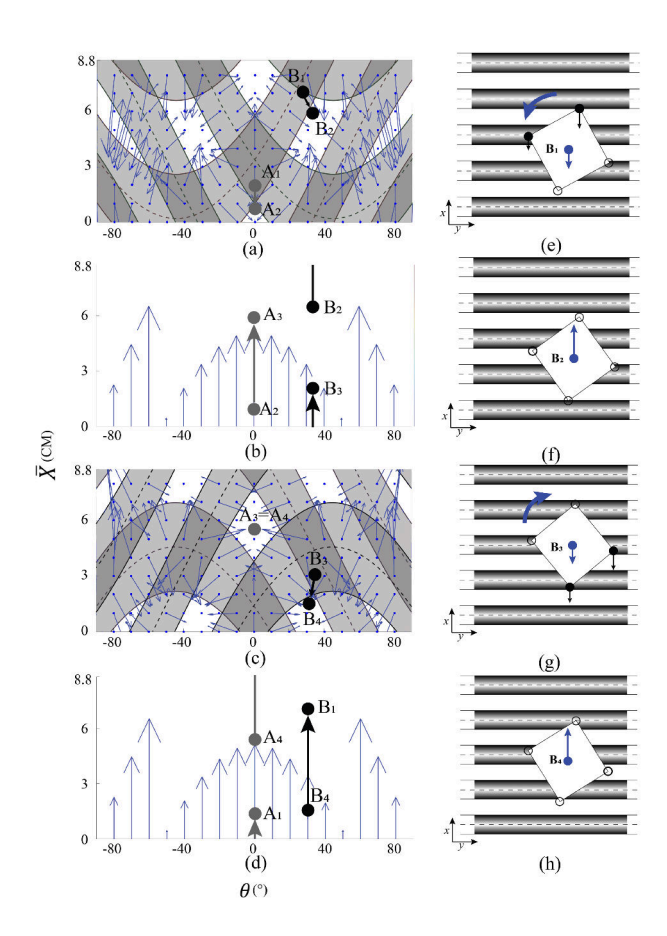


Fig. 9. State transition vectors for each mode (S_1, V_1, S_2, V_2) , from top to bottom) within a full stride for gait G_1 , illustrated in the robot's state space (a-d) and the world frame (e-h). (a, e) and (c, g) represent S_1 and S_2 , the slipping modes for {RF, LF} and {RH, LH} leg pairs, respectively. The state transition vectors for the slipping modes were computed as a sum of individual leg state transition vectors from Fig. 8. (b, f) and (d, h) represent V_1 and V_2 , the advancing modes for RF, LF and RH, LH leg pairs, respectively. States A_1 , A_2 , A_3 , A_4 and B_1 , B_2 , B_3 , B_4 represent the initial state of each mode for the steady state with $\theta_f = 0^\circ$ and $\theta_f = 35^\circ$, respectively. Color schemes are the same as Fig. 8.

leg positions) to be fully encoded in the (θ, \bar{X}) coordinate. With this representation, the robot's body-level dynamics under simultaneous or sequential leg-obstacle collisions can be directly computed and visualized in the state space, to facilitate the understanding of obstacle-modulated robot dynamics (Sec. IV-E, Sec. IV-F) and gait planning (Sec. V).

E. Model revealed mechanisms of gait-dependent steady states and enabled prediction of gait-dependent "funnel" outlets

The stride-wise return maps could explain the experimentally-observed passive robot orientations for different gaits. For the case illustrated in Fig. 9, we noticed that a robot that started at state A_1 would return to the same state after a full stride: $q(A_1) = F(q(A_1))$, where $q := (\theta, \bar{X})$ represents the robot state. Similarly, a robot that started at state B_1 would return to B_1 after each full stride. The orientation angles of A_1 and B_1 were 0° and 35° , the same angles as the robot was observed to passively converge to in our locomotion experiments (Fig. 5c, first row). We refer

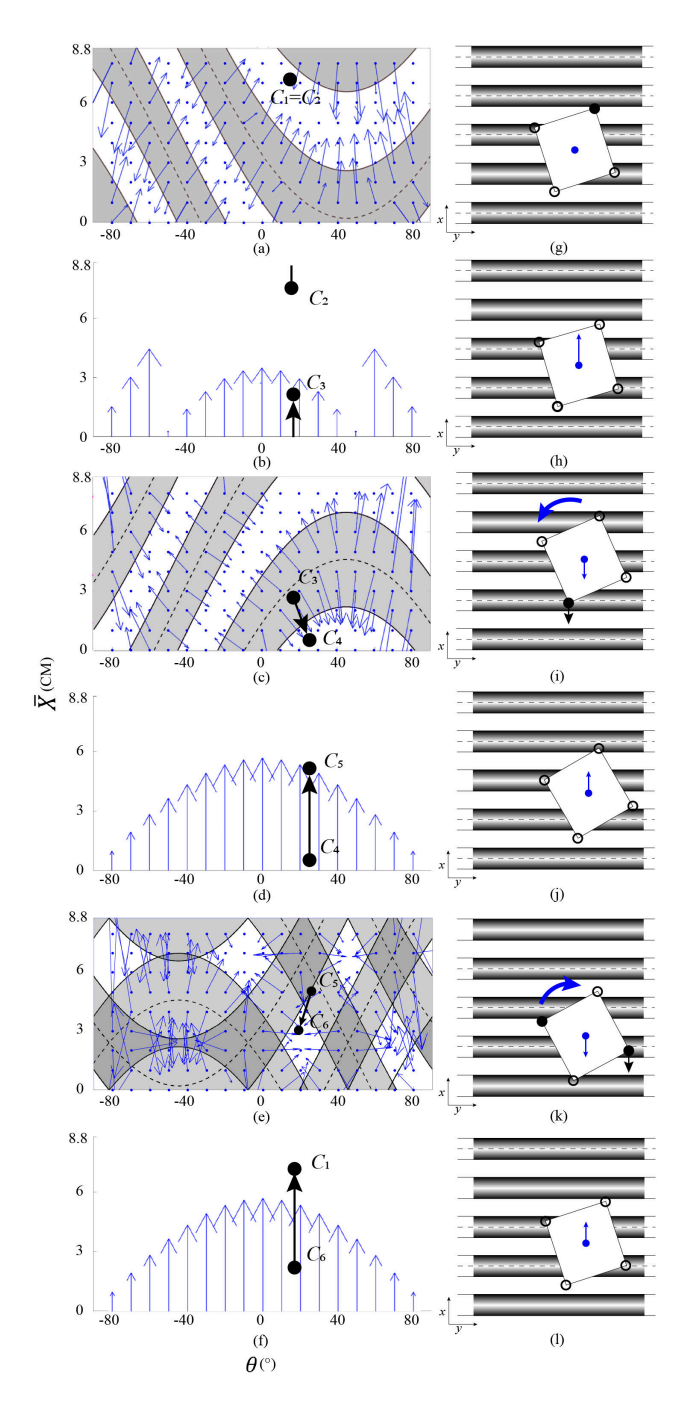


Fig. 10. State transition vectors for each mode $(S_1, V_1, S_2, V_2, S_3, V_3)$, from top to bottom) within a full stride for gait G_{11} , illustrated in the robot's state space (a-f) and the world frame (g-l). (a, g), (c, i) and (e, k) represent S_1, S_2 , and S_3 , the slipping modes for {RF}, {LH} and {LF, RH} legs, respectively. The state transition vectors for the slipping modes were computed as a sum of individual leg state transition vectors from Fig. 8. (b, h), (d, j), and (f, l) represent V_1, V_2 , and V_3 , the advancing modes for {RF}, {LH} and {LF, RH} legs, respectively. States $C_1, C_2, C_3, C_4, C_5, C_6$ represent the initial state of each mode for the steady state with $\theta_f = 19^\circ$. Color schemes are the same as Fig. 8.

to state A_1 and B_1 as the fixed points⁴ [35] of the discrete, obstacle-modulated robot dynamics. Similarly, stride-wise fixed points can be identified by solving q = F(q) for NVB gaits like G_{11} (Fig. 10, C_1).

For any general quadrupedal gait, $G = (\phi_1, \phi_2, \phi_3)$, we could use its return map, F, to theoretically determine the obstacle-modulated robot steady states. To do so, we construct a directed graph that represents the robot's state transition under repeated strides, following the method reported in [34]. Each node of the graph represents a robot state, whereas each directed edge represents the change of robot state within one stride (i.e., F). Once the directed graph was constructed, the robot's steady state could be identified by searching for selfmapping nodes within the graph [34]. Using this method, the steady state orientations could be predicted without having to perform numerical simulation from the beginning to the end, significantly reducing the computational effort required. This reduced computational effort could allow small, simple robots to assess obstacle interaction outcomes, and plan efficient strategies.

To validate the model-predicted steady states, we theoretically computed the steady-state orientation (Fig. 11, blue filled markers) for G_1 through G_{12} , and compared against the experiment-measured robot final orientations (Fig. 11, red histogram bands) from the 864 trials. The intensity of the red histogram bands represents the likelihood of experimentally observing an averaged final orientation, θ_f .

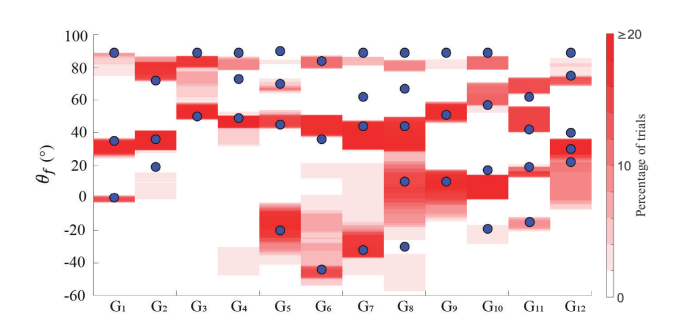


Fig. 11. Gait-dependent steady-state robot orientations for G_1 through G_{12} . Blue markers represent model predicted stride-wise steady orientation, whereas the red histogram bands represent the experimentally measured robot steady orientation from the 864 trials, averaged for the last two gait cycles. Experimental data for each gait include all 16 initial orientations tested. The color scale of the red histogram bands represents the percentage of trials for each gait where the θ_f was observed, whereas deeper red represents a larger percentage.

The model-predicted steady-state robot orientations agreed well with the experimental measurements for all general gaits tested: the majority of high-intensity red histogram bands are located within the adjacency (*i.e.*, within 10°) of the predicted steady-state orientations. We note that there were a few model-predicted steady-state orientations that were not observed from our experiments (e.g., G_7 , 62° ; G_8 , 67°). This is likely because the basins of attraction [35] of these steady

⁴For all results reported in this paper, the Poincare section of the return map was defined as the beginning of the RF leg stance phase.

states were relatively small⁵, and therefore the probability of observing these steady states in experiments was low. With the basin of attraction analysis reported in Sec. IV-F, one could identify these steady states that were less likely to observe experimentally.

These model-predicted steady states explained the experimentally-observed dependence of passive robot orientation on gaits (Sec. III-A), and allowed theoretical prediction of these gait-dependent passive orientations. For a small robot navigating in a field with densely-distributed large, slippery obstacles, a model that can predict these passively-stable orientations is extremely useful: knowing the mapping from each gait to the passively-stable orientation angle enabled by that gait, the robot does not have to "fight against" the large obstacle disturbances, but instead could simply execute a fixed gait to passively "flow" towards a desired moving direction. For example, with a gait G_1 , a robot starting at 50° could passively flow to 35°, whereas a gait G_3 would let the robot passively flow back from 35° to 50°. Similarly, a robot could use a sequence of gaits to flexibly change its moving directions, and follow desired paths among the large, slippery obstacles, through the utilization of obstacle disturbances (Sec. V).

F. Model revealed steady state convergence dynamics and enabled the computation of basins of attractions (funnel "inlets")

In addition to predicting the steady states (*i.e.*, "funnel outlets"), the state transition vectors could also help reveal how robot states converge from an initial state to the experimentally-observed steady state, and determine the basins of attraction associated with each steady state. The basins of attraction referred to the set of initial states that can passively converge to each steady state (*i.e.*, "funnel inlets" in Fig. 2).

Take gait G_1 as an example, Fig. 12a(i) - a(vii) visualizes how the distribution of robot states (colored points) evolved over time. Following the state transition vectors, a robot starting from all possible initial states (Fig. 12 a-(i)) would quickly converge to few localized regions in the state space (Fig. 12 a, (iv) to (vii)). The orientation of these converged states (0°, $\pm 35^{\circ}$, and $\pm 90^{\circ}$) were consistent with experiment-observed θ_f . To visualize the collection of initial states that converged to the same orientation, we colored the initial states in Fig. 12a-(i) based on the orientation of the final state that they would converge to. These colored regions marked the basins of attractions (funnel inlets) for the corresponding steady state (funnel outlets). The predicted basins of attractions (Fig. 13 colored regions) agreed well with experiment measurements (Fig. 6).

The basins of attraction explained the experimentally-observed dependence of robot final orientations on its initial states (Fig. 6). Fig. 12b,c shows the experiment recording of a robot starting from two different initial states: $(\theta, \bar{X}) = (20^{\circ}, 8.8 \text{cm})$ (corresponding to marker A in Fig. 12a-(i)), and $(\theta, \bar{X}) = (20^{\circ}, 6.0 \text{cm})$ (corresponding to marker B in Fig. 12a-(i)). According to the predicted basins of attraction, a robot

with initial state A would converge to a final orientation of 0° , whereas with initial state B the robot would converge to 35° . This is consistent with the experimental observations (Fig. 12b, c). Using this prediction, we could also infer the robustness of each steady state: steady states with large basins of attraction may be less sensitive to intrinsic noises in the experiments, allowing simple robots to robustly navigate complex terrains by utilizing obstacle-interacting forces.

V. OBSTACLE-AIDED NAVIGATION BY COMPOSING GAIT FUNNELS

In this section, we demonstrate that using different gaits, a robot could "select" different funnels and "passively" converge to different orientation angles under the obstacle forces without needing any external steering.

A. Sequential connection of gait "funnels" to achieve desired shape trajectory

The gait-dependent steady states offered a robust way for robots to passively (*i.e.*, without body-level steering) converge to desired orientations. We hypothesize that by sequentially switching through a number of gaits, a legged robot could efficiently generate desired trajectory by utilizing obstacle-interaction forces. This is especially useful for environments where obstacle sizes are large as compared to robot leg size, where it is challenging to treat obstacle forces as small disturbances. In addition, since the steady states are stable and are attracted from nearby states, the method is less sensitive to sensor and actuator noises and therefore offers a great opportunity for small robots with limited sensing and actuation resources.

To select the gait sequence for the desired trajectory, we search through the directed graph that encoded the model-predicted steady states and associated basins of attractions from Sec. IV, following method developed in [34]. Although with only three specific virtual bipedal gaits, [34] demonstrated that the directed graph based gait planner can successfully identify possible gait sequences to connect from a given initial robot state to a desired goal robot state.

Here we extend the graph based gait planner to include any general quadrupedal gaits, (ϕ_1, ϕ_2, ϕ_3) , for obstacle-aided locomotion and navigation. For each gait, steady state orientations (funnel outlets) and associated basins of attractions (funnel inlets) could be determined using the method discussed in Sec. IV-E and Sec. IV-F. The gait planner then searched for a sequence of funnels that when connected sequentially (Fig. 2) could allow the robot state to passively "flow" from a given initial state to a desired end state.

To experimentally validate the effectiveness of the sequential gait composition method for obstacle-aided navigation, we challenged the robot to produce three different shapes of trajectories, letter "U", "S", and "C" (Fig. 14b) while across the obstacle field, without any body-level steering. The obstacle distribution and the initial state of the robot, (θ_0, \bar{X}_0) , were given to the robot prior to the trial. Using the model-predicted steady states (Fig. 11 blue markers) and their corresponding basins of attractions (Fig. 13 colored regions)

⁵Simulation results suggested that the boundary of basins of attractions were only 5° from the steady-state orientation

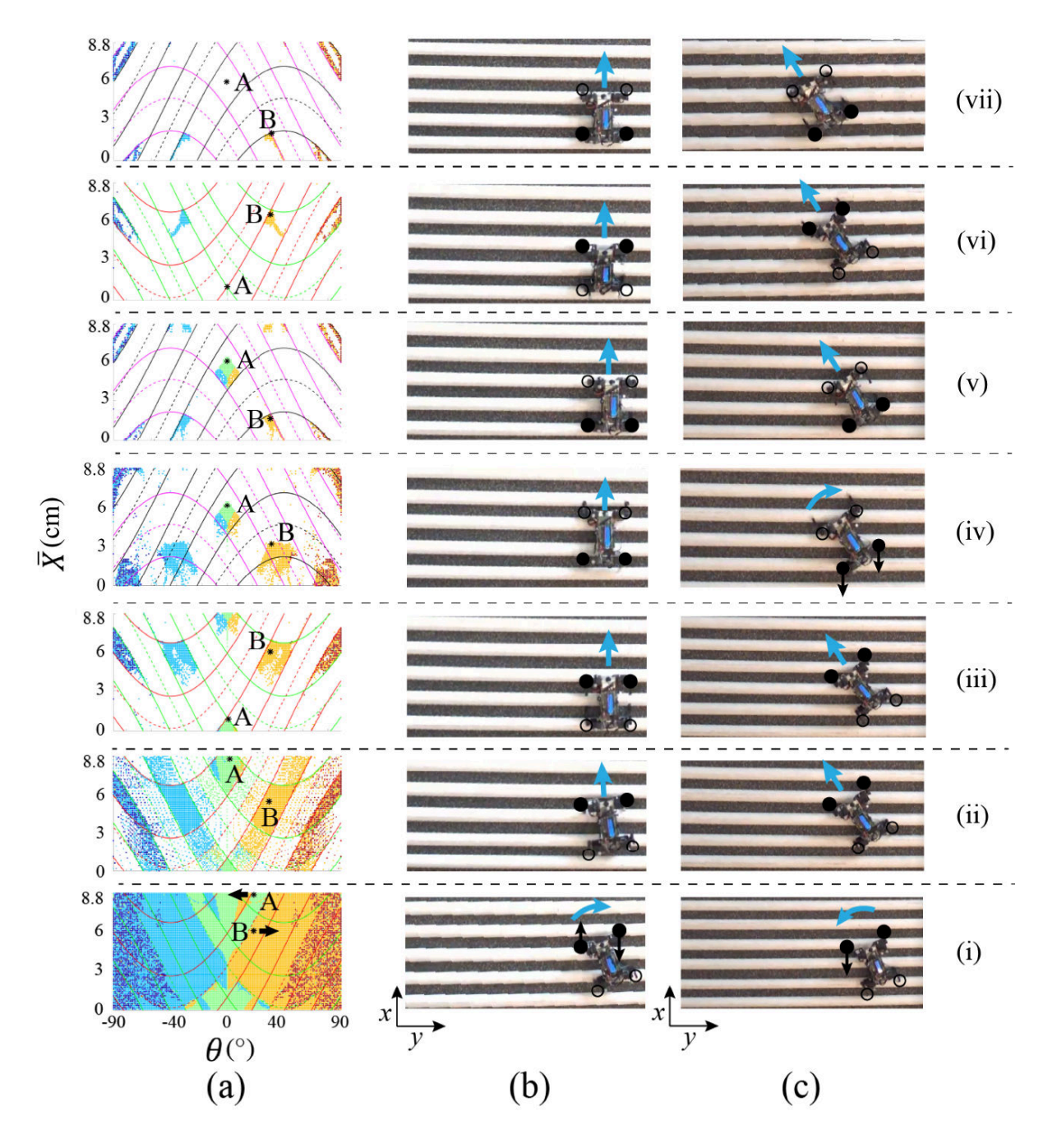


Fig. 12. Robot state transitions for a representative gait, G_1 , computed using the state transition vectors (a), and recorded from experiments (b, c). Colored points in (a), from bottom to top plots, represent the evolving robot states, (θ, \bar{X}) , at t = 0s, 0.05s, 0.3s, 1.5s, 1.8s, 3.3s, 4.8s, respectively. Marker colors represent different initial states that converge to the same steady-state orientation. Solid and dashed curves represent obstacle edges and center, respectively, projected in the robot state space. Curve color represents the obstacle projection relative to different robot legs: red, green, purple, and black corresponding to LF, RF, RH, and LH legs, respectively. Markers A and B in (a) represent two initial robot states with the same orientation ($\theta_0 = 20^\circ$) and initial positions only 2.8cm apart, but converged to two different steady-state orientations, 0° and 35° , respectively. Image sequences in (b) and (c) were recorded from the two experiment trials with initial conditions corresponding to markers A and B in (a), respectively. Solid black circles represent legs in the stance phase, whereas empty black circles represent legs in the swing phase. Black arrows indicate the obstacle forces exerted on each individual leg, and blue arrows indicate the direction of robot orientation change due to obstacle forces.

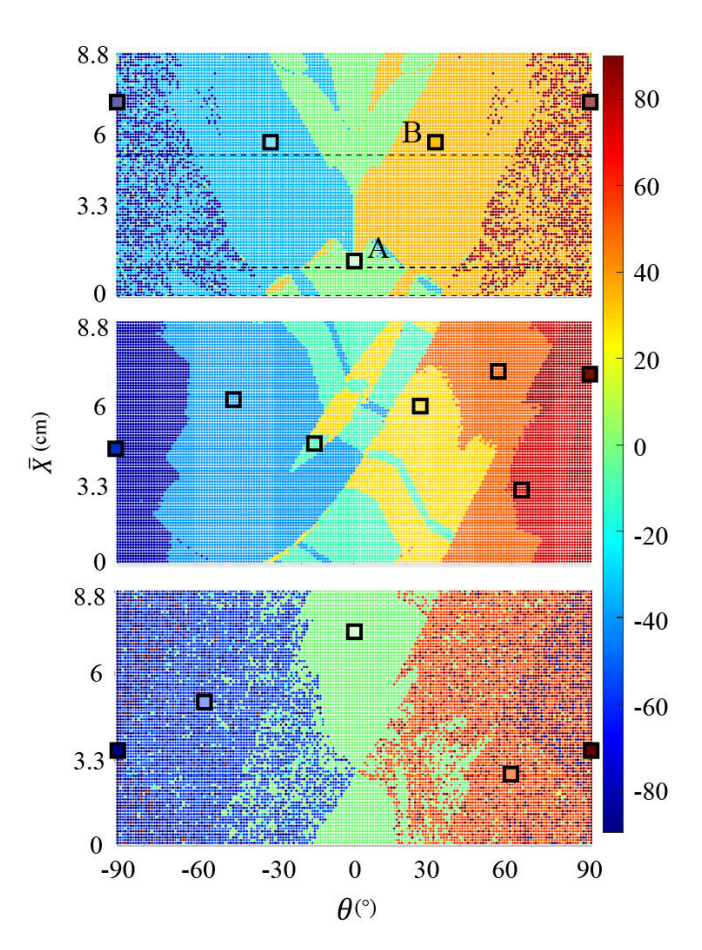


Fig. 13. Computed basins of attraction for G_1 , G_1 , G_9 , shown from top to bottom, respectively. Black squares represent model-predicted steady states determined through the stride-wise return map. Colored regions represent basins of attraction associated with each steady state. Colors represent the orientation angles of the corresponding steady states. The three horizontal dashed lines in the top plot marked $\bar{X}_0 = 0$ cm, 1cm, 5cm, corresponding to the experiment initial conditions reported in Fig. 6.

for the twelve gaits, G_1 through G_{12} , the robot planned its gait sequence for each desired trajectory before the traverse.

The planned gait sequence for the "S"-shaped trajectory, $G_{11} \rightarrow G_6 \rightarrow G_1 \rightarrow G_{11} \rightarrow G_1 \rightarrow G_5 \rightarrow G_6$, is illustrated in Fig. 14a. The required initial state for the "S"-shaped trajectory was $\theta_0 = 70^\circ$, $\bar{X}_0 = 3$ cm (Fig. 14a, state a). The model predicted that a G_{11} gait could allow the robot to passively converge to $\theta_1^* = 62^{\circ}$ (Fig. 14a, state b). Since state b is within the basin of attraction of the next funnel (Fig. 14a, orange region on G_6 layer), the next planned gait, G_6 , would send the robot to $\theta_2^* = 39^\circ$ (Fig. 14a, state c). Similarly, the robot subsequently switched through gaits G_1 , G_{11} , G_1 , G_5 , and G_6 , as its orientation "flowed" through the predicted "funnel outlets" (i.e., steady-state orientations of each gait): $\theta_3^* = 0^\circ$ (Fig. 14a, state d), $\theta_4^* = -19^\circ$ (Fig. 14a, state e), $\theta_5^* = -36^\circ$ (Fig. 14a, state f), $\theta_6^* = -17^\circ$ (Fig. 14a, state g), and $\theta_7^* = 39^\circ$ (Fig. 14a, state h), respectively. This illustrates the "funnel" concept depicted in Fig. 2: the outlet of each gait "funnel" resides in the inlet of the next gait (e.g., , Fig. 14a, state glocated within the cyan regions on the G_5 layer); as such, by connecting these funnels one after another, the robot state was constrained to flow through the desired waypoint states under the modulation of obstacle forces.

Similar to the "S"-shaped trajectory, the gait planner returned two different gait sequences: $G_1 \rightarrow G_{11} \rightarrow G_6 \rightarrow G_5 \rightarrow G_1$ for the "U" shaped trajectory, and $G_{11} \rightarrow G_6 \rightarrow G_1 \rightarrow G_1 \rightarrow G_6 \rightarrow G_1$ for the "C" shaped trajectory. Robot trajectories recorded from the experiment (Fig. 14b) demonstrated that the robot was able to successfully produce all three desired trajectories simply by sequentially executing the planned gaits.

We highlight that during the entire trial, no external sensing or body-level steering was adopted. The robot simply executed the planned gait in sequence, *i.e.*, performing each gait for 3 strides before switching to the next. This demonstrated that with the ability to predict the interaction outcomes of legobstacle interactions, even an extremely simple robot could effectively follow desired paths through the densely distributed large obstacles (with diameters comparable with the robot leg size). We also note that in Sec. III we only performed experiments for initial orientations between 0 - 75 degrees, but in the demonstration, the planner used model-predicted steady states and initial states beyond this range. For these states, we didn't have any experiment data, and the planner solely relied on our model prediction. This spoke to the predictive power of our reduced-complexity model.

B. Extending the method to non-evenly-spaced obstacle field

In this section, we demonstrate how our method can be extended beyond the simplified setting of evenly-spaced obstacles. To do so, we challenged the robot to produce the same "S"-shaped trajectory on a "slow-varying" obstacle field with non-evenly-spaced obstacles. The new obstacle field consisted of 4 segments, each segment containing 7 semi-cylindrical obstacles. The obstacle spacing for the 4 segments were set to different values: 2cm, 4cm, 5cm, and 7cm (Fig. 15a).

For regions within the same obstacle spacing (i.e., $X < X_D - C$ and $X > X_D + C$, where X_D represents the starting position of the new segment, and C is the robot's half diagonal length), the same method from Sec. IV and Sec. V could be directly applied to compute the return map and perform the gait planning.

For regions where the obstacle spacing varies from one to another (i.e., $X \in [X_D - C, X_D + C)$), steady-state orientations would no longer exist. However, the state transition vectors could be computed in a similar manner to guide the gait planning. As an example, the green rectangle in Fig.15b highlights a representative region of varying obstacle spacing, where the two legs (LF and RF) were within the 4cm spacing region, and the other two legs (LH and RH) were within the 2cm spacing region. Due to the varying obstacle spacing, the obstacle force, $F_i(X_i)$, would exhibit different distribution for each leg. However, the state transition vectors for each leg could still be computed by integrate Eqn. 3 and Eqn. 4, as illustrated in Sec. IV. Fig. 15c visualizes the state transition vectors corresponding to the scenario shown in Fig. 15b. For a given gait, G, these state transition vectors could be composed to construct the directed graph for the transitional region. With

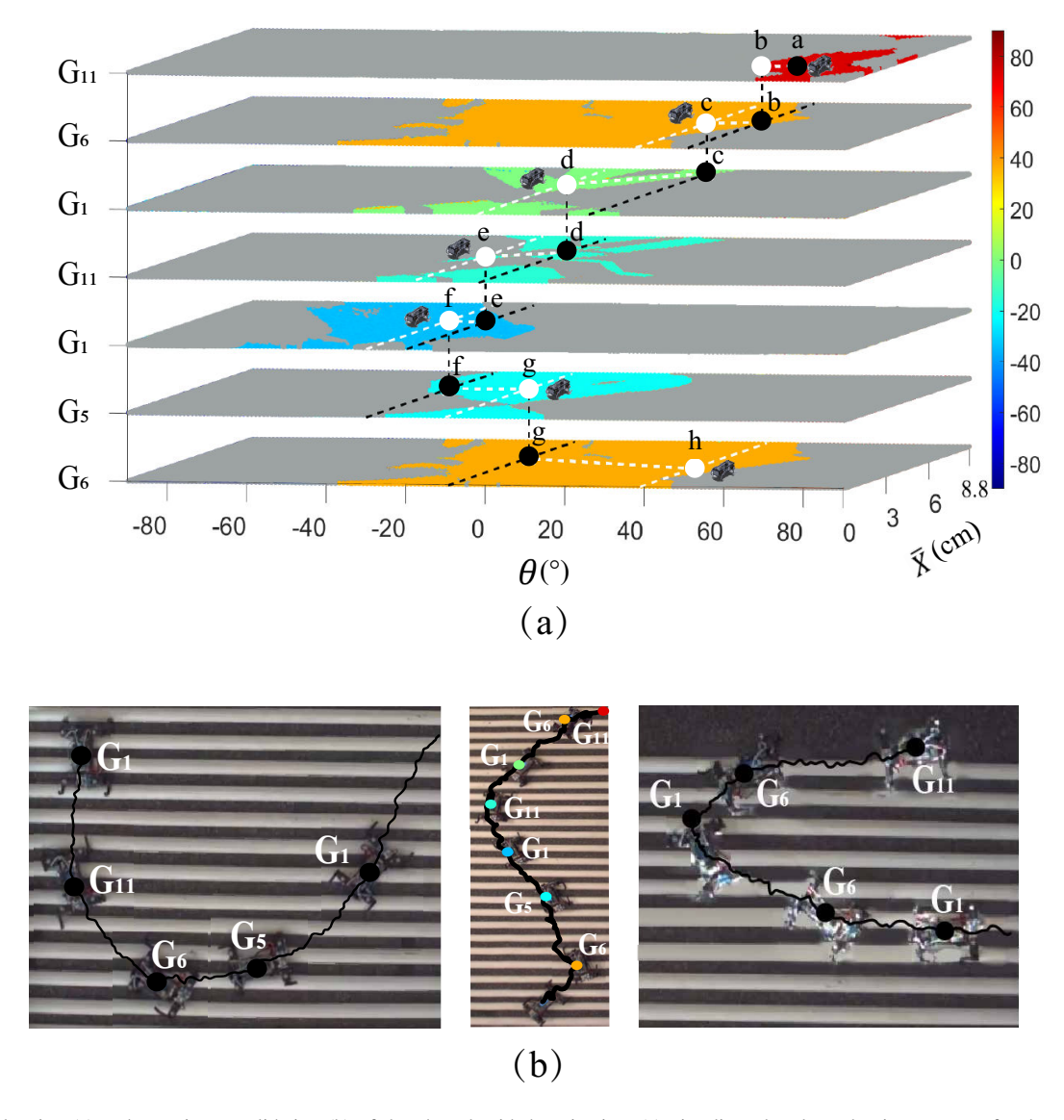


Fig. 14. The planning (a) and experiment validation (b) of the obstacle-aided navigation. (a) visualizes the planned gait sequences for the robot to achieve an "S"-shaped trajectory. From top to bottom, each layer represents one gait: $G_{11} \rightarrow G_6 \rightarrow G_1 \rightarrow G_{11} \rightarrow G_1 \rightarrow G_5 \rightarrow G_6$. The white circular markers on each layer represent the predicted robot's steady state under repeated obstacle collisions by maintaining the specific gait. The colored regions surrounding the white circles represent the predicted basins of attraction of the steady state, *i.e.*, the set of initial states that would be "attracted" to the steady state. The colors of the basins of attraction represent the robot orientation angle at the steady state, as shown in the color bar. The three images in (b) show the experimentally-recorded robot trajectories across the obstacle field for the three desired paths: "U", "S", and "C". The solid black line is the experimentally-recorded robot trajectory in the world frame, tracked by the motion capture cameras.

the directed graph, the same method from Sec. V could be applied to search for the gait sequence that takes the robot's initial state to the desired state, for a desired trajectory.

We experimentally tested the robot's trajectory across this slow-varying obstacle field, with the model-planned gait sequence: $G_7 \rightarrow G_3 \rightarrow G_1 \rightarrow G_3 \rightarrow G_1 \rightarrow G_7$. The gait sequence was pre-programmed in the robot, and the robot simply switched to the subsequent gait once a fixed number of strides were completed. Experimentally-measured robot trajectory (Fig. 15a) demonstrated that our method applied well on the slow-varying obstacle field, allowing the robot to produce the desired trajectory by utilizing obstacle disturbances.

This experiment demonstrated the feasibility for our meth-

ods to be extended beyond the simplified setting. Going forward, for environments with more rapidly-varying obstacle distributions, the state transition vectors and the open-looped robot gaits to achieve a desired moving direction could be computed similarly for a finite spatial segment (e.g., a few steps ahead), and updated over time. For completely randomized obstacle distribution, steady states would no longer exist. As such, achieving robust open-loop navigation would require a better understanding of the transitional dynamics. The method to compute state transition vectors provided a starting point to model the transitional dynamics, and to assess the sensitivity of a trajectory to sensor and actuator noises.

VI. CONCLUSION

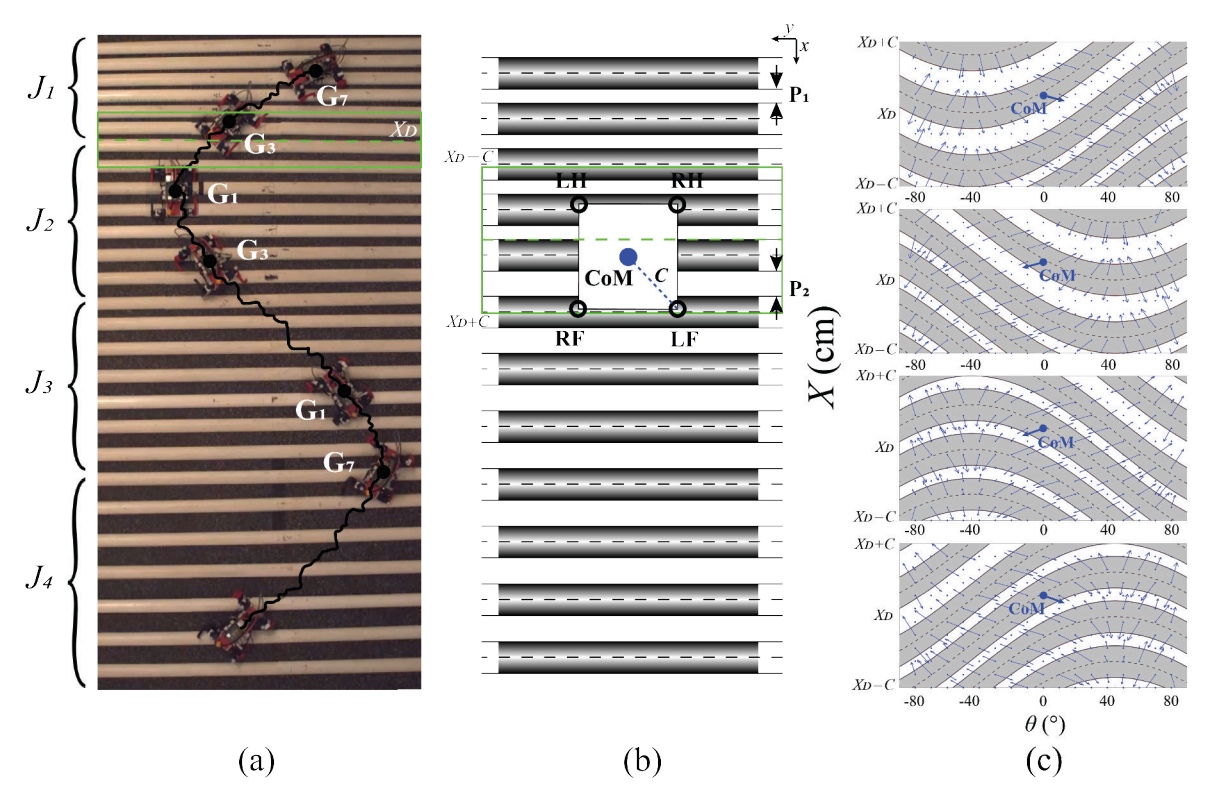


Fig. 15. The experiment demonstration of obstacle-aided trajectory control across unevenly-spaced obstacles. (a) The "slow-varying" obstacle field consisting of four segments of different spacing: 2 cm within J_1 , 3cm within J_2 , 5 cm within J_3 , and 7 cm within J_4 . Black line represents the experimentally-measured robot trajectory across the obstacle field using the planned gait sequence: $G_7 \to G_3 \to G_1 \to G_3 \to G_1 \to G_7$. (b) A schematic corresponding to the obstacle area within the green box in (a), where LF, RF legs were within the obstacle region with spacing P_2 and LH, RH legs within the obstacle area with spacing P_1 . The green dash line marks the division line between two segments, denoted as X_D . (c) The state transition vectors corresponding to the green box zone marked in (a) and (b), for RF, LF, LH, RH leg from top to bottom.

The results presented in this paper revealed how different gaits allow a multi-legged robot to elicit different interaction forces from its environment. Furthermore, we show that this understanding can allow a simple robot to plan gait sequences to move towards desired directions by utilizing obstacle disturbances. This opens a new avenue for simple, low-cost robots to cope with environments with large obstacles and perturbations: instead of relying on canceling these large perturbations, a simple robot could actively utilize these disturbances and collisions to produce desired dynamics.

While this paper is still a beginning step towards the vision of "obstacle-aided locomotion and navigation", the results from this paper could be applied to guide the morphological and gait parameter selections for a variety of simple robots [37], [38], [39] for them to effectively traverse their environments with minimal sensing and computation. Even for robots with better sensing and computation capabilities, the understandings of robot-environment interaction could allow environment to become part of the control resources, to improve their locomotion effectiveness on complex terrains. In addition, we envision that our results could help explore questions beyond robotics, such as to explain animals' gait adaptation behaviors on rough terrain [31]. These explorations could in turn inspire simple strategies for robots to navigate challenging environments.

Given the simplicity of the model and the robustness of the

results, we envision that continued expansion on this "obstacleaided locomotion" strategy could open up many new avenues, enabling future robots to flexibly interact with a variety of complex real-world environments such as rocky hills, forests, and earthquake rubble.

ACKNOWLEDGMENT

This work is supported by funding from the National Science Foundation (NSF) CAREER award #2240075, the NASA Planetary Science and Technology Through Analog Research (PSTAR) program, Award # 80NSSC22K1313, and the NASA Lunar Surface Technology Research (LuSTR) program, Award # 80NSSC24K0127. The authors would like to thank Elijah Yap for helping design and program the robot, Kaustav Chakraborty, Alexander Kao-Sowa, and Simon To for helping with preliminary data collection, and Matthew Kvalheim for helpful discussions.

REFERENCES

- [1] J. Casper and R. Murphy, "Human-robot interactions during the robot-assisted urban search and rescue response at the world trade center," *IEEE Transactions on Systems, Man, and Cybernetics, Part B (Cybernetics)*, vol. 33, no. 3, pp. 367–385, 2003.
- [2] C. Li and K. Lewis, "The need for and feasibility of alternative ground robots to traverse sandy and rocky extraterrestrial terrain," Advanced Intelligent Systems, p. 2100195, 2022.
- [3] F. Qian and D. I. Goldman, "The dynamics of legged locomotion in heterogeneous terrain: universality in scattering and sensitivity to initial conditions." in *Robotics: Science and Systems*, 2015, pp. 1–9.

- [4] F. Qian and D. Goldman, "Anticipatory control using substrate manipulation enables trajectory control of legged locomotion on heterogeneous granular media," in *Micro-and Nanotechnology Sensors, Systems, and Applications VII*, vol. 9467. International Society for Optics and Photonics, 2015, p. 94671U.
- [5] C. Li, A. O. Pullin, D. W. Haldane, H. K. Lam, R. S. Fearing, and R. J. Full, "Terradynamically streamlined shapes in animals and robots enhance traversability through densely cluttered terrain," *Bioinspiration & biomimetics*, vol. 10, no. 4, p. 046003, 2015.
- [6] S. W. Gart and C. Li, "Body-terrain interaction affects large bump traversal of insects and legged robots," *Bioinspiration & biomimetics*, vol. 13, no. 2, p. 026005, 2018.
- [7] J. Schulman, J. Ho, A. X. Lee, I. Awwal, H. Bradlow, and P. Abbeel, "Finding locally optimal, collision-free trajectories with sequential convex optimization." in *Robotics: science and systems*, vol. 9. Citeseer, 2013, pp. 1–10.
- [8] H.-W. Park, P. M. Wensing, and S. Kim, "Jumping over obstacles with mit cheetah 2," *Robotics and Autonomous Systems*, vol. 136, p. 103703, 2021
- [9] D. E. Koditschek and E. Rimon, "Robot navigation functions on manifolds with boundary," *Advances in applied mathematics*, vol. 11, no. 4, pp. 412–442, 1990.
- [10] P. Vadakkepat, K. C. Tan, and W. Ming-Liang, "Evolutionary artificial potential fields and their application in real time robot path planning," in *Proceedings of the 2000 congress on evolutionary computation. CEC00* (Cat. No. 00TH8512), vol. 1. IEEE, 2000, pp. 256–263.
- [11] L. Lapierre, R. Zapata, and P. Lepinay, "Combined path-following and obstacle avoidance control of a wheeled robot," *The International Journal of Robotics Research*, vol. 26, no. 4, pp. 361–375, 2007.
- [12] G. Mester, "Obstacle-slope avoidance and velocity control of wheeled mobile robots using fuzzy reasoning," in 2009 International Conference on Intelligent Engineering Systems. IEEE, 2009, pp. 245–249.
- [13] M. H. Raibert, Legged robots that balance. MIT press, 1986.
- [14] U. Saranli, M. Buehler, and D. E. Koditschek, "Rhex: A simple and highly mobile hexapod robot," *The International Journal of Robotics Research*, vol. 20, no. 7, pp. 616–631, 2001.
- [15] S. Kim, J. E. Clark, and M. R. Cutkosky, "isprawl: Design and tuning for high-speed autonomous open-loop running," *The International Journal* of Robotics Research, vol. 25, no. 9, pp. 903–912, 2006.
- [16] J. K. Yim and R. S. Fearing, "Precision jumping limits from flight-phase control in salto-1p," in 2018 IEEE/RSJ international conference on intelligent robots and systems (IROS). IEEE, 2018, pp. 2229–2236.
- [17] P. Birkmeyer, K. Peterson, and R. S. Fearing, "Dash: A dynamic 16g hexapedal robot," in 2009 IEEE/RSJ international conference on intelligent robots and systems. IEEE, 2009, pp. 2683–2689.
- [18] K. Hauser, T. Bretl, J.-C. Latombe, K. Harada, and B. Wilcox, "Motion planning for legged robots on varied terrain," *The International Journal* of Robotics Research, vol. 27, no. 11-12, pp. 1325–1349, 2008.
- [19] B. Sebastian and P. Ben-Tzvi, "Active disturbance rejection control for handling slip in tracked vehicle locomotion," *Journal of Mechanisms* and Robotics, vol. 11, no. 2, p. 021003, 2019.
- [20] J. Buchli, M. Kalakrishnan, M. Mistry, P. Pastor, and S. Schaal, "Compliant quadruped locomotion over rough terrain," in 2009 IEEE/RSJ international conference on Intelligent robots and systems. IEEE, 2009, pp. 814–820.
- [21] J. Aguilar, T. Zhang, F. Qian, M. Kingsbury, B. McInroe, N. Mazouchova, C. Li, R. Maladen, C. Gong, M. Travers et al., "A review on locomotion robophysics: the study of movement at the intersection of robotics, soft matter and dynamical systems," *Reports on Progress in Physics*, vol. 79, no. 11, p. 110001, 2016.
- [22] N. H. Hunt, J. Jinn, L. F. Jacobs, and R. J. Full, "Acrobatic squirrels learn to leap and land on tree branches without falling," *Science*, vol. 373, no. 6555, pp. 697–700, 2021.
- [23] Y. Han, R. Othayoth, Y. Wang, C.-C. Hsu, R. de la Tijera Obert, E. Francois, and C. Li, "Shape-induced obstacle attraction and repulsion during dynamic locomotion," *The International Journal of Robotics Research*, vol. 40, no. 6-7, pp. 939–955, 2021.
- [24] D. Ramesh, A. Kathail, D. E. Koditschek, and F. Qian, "Modulation of robot orientation via leg-obstacle contact positions," *IEEE Robotics and Automation Letters*, vol. 5, no. 2, pp. 2054–2061, 2020.
- [25] P. E. Schiebel, J. M. Rieser, A. M. Hubbard, L. Chen, D. Z. Rocklin, and D. I. Goldman, "Mechanical diffraction reveals the role of passive dynamics in a slithering snake," *Proceedings of the National Academy of Sciences*, vol. 116, no. 11, pp. 4798–4803, 2019.
- [26] J. M. Rieser, P. E. Schiebel, A. Pazouki, F. Qian, Z. Goddard, K. Wiesenfeld, A. Zangwill, D. Negrut, and D. I. Goldman, "Dynamics of

- scattering in undulatory active collisions," *Physical Review E*, vol. 99, no. 2, pp. 17–19, 2019.
- [27] T. Wang, C. Pierce, V. Kojouharov, B. Chong, K. Diaz, H. Lu, and D. I. Goldman, "Mechanical intelligence simplifies control in terrestrial limbless locomotion," arXiv preprint arXiv:2304.08652, 2023.
- [28] R. R. Burridge, A. A. Rizzi, and D. E. Koditschek, "Sequential composition of dynamically dexterous robot behaviors," *The International Journal of Robotics Research*, vol. 18, no. 6, pp. 534–555, 1999.
- [29] G. C. Haynes, A. A. Rizzi, and D. E. Koditschek, "Multistable phase regulation for robust steady and transitional legged gaits," *The Interna*tional Journal of Robotics Research, vol. 31, no. 14, pp. 1712–1738, 2012.
- [30] S. Revzen and J. M. Guckenheimer, "Estimating the phase of synchronized oscillators," *Physical Review E*, vol. 78, no. 5, p. 051907, 2008.
- [31] S. Wilshin, M. A. Reeve, G. C. Haynes, S. Revzen, D. E. Koditschek, and A. J. Spence, "Longitudinal quasi-static stability predicts changes in dog gait on rough terrain," *Journal of Experimental Biology*, vol. 220, no. 10, pp. 1864–1874, 2017.
- [32] M. Hildebrand, "The quadrupedal gaits of vertebrates," *Bioscience*, vol. 39, no. 11, p. 766, 1989.
- [33] F. Qian and D. E. Koditschek, "An obstacle disturbance selection framework: emergent robot steady states under repeated collisions," *The International Journal of Robotics Research*, p. 0278364920935514.
- [34] K. Chakraborty, H. Hu, M. D. Kvalheim, and F. Qian, "Planning of obstacle-aided navigation for multi-legged robots using a samplingbased method over directed graphs," *IEEE Robotics and Automation Letters*, vol. 7, no. 4, pp. 8861–8868, 2022.
- [35] S. H. Strogatz, Nonlinear dynamics and chaos: with applications to physics, biology, chemistry, and engineering. CRC press, 2018.
- [36] M. Brin and G. Stuck, Introduction to dynamical systems. Cambridge university press, 2002.
- [37] P. E. Schiebel, J. Shum, H. Cerbone, and R. J. Wood, "An insect-scale robot reveals the effects of different body dynamics regimes during openloop running in feature-laden terrain," *Bioinspiration & Biomimetics*, vol. 17, no. 2, p. 026006, 2022.
- [38] H. Kabutz and K. Jayaram, "Design of clari: A miniature modular origami passive shape-morphing robot," Advanced Intelligent Systems, vol. 5, no. 12, p. 2300181, 2023.
- [39] X. A. Wu, T. M. Huh, A. Sabin, S. A. Suresh, and M. R. Cutkosky, "Tactile sensing and terrain-based gait control for small legged robots," *IEEE Transactions on Robotics*, vol. 36, no. 1, pp. 15–27, 2019.



Haodi Hu received the B.Eng. degree in electronic information engineering from Northeast Forest University, Harbin, China, in 2019 and the M.S. degree in electrical engineering from the University of Southern California, Los Angeles, U.S., in 2021. He is currently a Ph.D. Student at RoboLand lab advised by Prof. Feifei Qian in Viterbi School of Engineering at the University of Southern California. His research interests include legged robot locomotion and navigation, motion planning, robot learning, multiagent robot cooperation, and robot manipulation.



Feifei Qian received her PhD in Electrical Engineering and M.S. in Physics from the Georgia Institute of Technology, Atlanta, GA, USA, in 2015 and 2011, respectively. She is currently an Assistant Professor in the Ming Hsieh Department of Electrical Engineering at the University of Southern California (USC), Los Angeles, CA, USA. Before joining USC, she worked as a postdoctoral researcher at the GRASP lab, University of Pennsylvania, Philadelphia, PA, USA, from 2016 to 2019. Her research interests include bio-inspired robotics, legged loco-

motion, terrain mechanics, proprioceptive sensing and human-robot teaming with applications to robot-aided earth and planetary explorations. She served as the Associated Editor for the 2023 IEEE International Conference on Robotics and Automation (ICRA), and the Program Committee for the 25th International Conference on Climbing and Walking Robots (CLAWAR).